Lane-consistent, semimicroscopic nucleon-nucleus optical model

E. Bauge, J. P. Delaroche, and M. Girod
Commissariat à l'Energie Atomique, Service de Physique Nucléaire, Boıte Postale 12, F-91680 Bruyères-le-Châtel, France
(Received 29 September 2000; published 22 January 2001)

A semimicroscopic, Lane-consistent optical model is established up to 200 MeV for nucleons incident on spherical and near-spherical nuclei with masses $40 \leqslant A \leqslant 209$. This model, based on the earlier approach of Jeukenne, Lejeune, and Mahaux in nuclear matter, is an extension of our previous work [E. Bauge, J. P. Delaroche, and M. Girod, Phys. Rev. C **58**, 1118 (1998)]. The modulus of the isovector potential is extracted and compared with measurements and fully microscopic predictions. Good overall descriptions of nucleon scattering, of transitions to isobaric analog states, and of reaction observables are obtained down to 1 keV. Those results are discussed in detail.

DOI: 10.1103/PhysRevC.63.024607 PACS number(s): 24.10.Ht, 25.40.Kv, 25.40.Cm, 25.40.Dn

I. INTRODUCTION

In recent years, the microscopic and semimicroscopic approaches to the optical model potential (OMP) have successfully explained the scattering of nucleons from nuclei of diverse masses [1–5], as well as of heavy ion (HI) scattering [6]. All these approaches have in common the fact that they rely on folding a nucleon-nucleon (N-N) effective interaction with nuclear structure information describing the target nucleus (as well as the projectile nucleus for HI collisions), and many rely on Brückner-Hartree-Fock (BHF) theory [7] to construct a density-dependent effective interaction from realistic free nucleon-nucleon forces. The works of Jeukenne, Lejeune, and Mahaux (JLM) [8–11], upon which the present approach is based, used this BHF framework to calculate a mass operator in nuclear matter (NM) from the Reid hard core [12] free N-N interaction. This mass operator can be assimilated to the OMP in NM [13]. Once put on the energy shell, the NM OMP was parametrized [11] in a convenient form for energies up to 160 MeV, and can be applied to finite nuclei via the improved local density approximation (ILDA). In Ref. [5], the energy range of the JLM OMP was extended to 200 MeV, and the energy variations of the potential depth were empirically tuned and parametrized, separately for proton and neutron projectiles, to reproduce scattering and reaction observables for spherical and quasispherical nuclei between ^{40}Ca and ^{209}Bi. Thus Ref. [5] defined a new semimicroscopic (SM) OMP, using a density dependence very close to that of the original JLM potential, as well as a phenomenologically adjusted energy dependence, and gave an optimal choice of the ILDA parameters. In Refs. [14–16], this SM OMP was extended to permanently deformed nuclei in the rare earth region and to soft, deformable stable and unstable S and Ar isotopes, respectively.

However, while the JLM approach is Lane consistent [17] by definition [Eq. (10) of Ref. [11]], many comparisons with experimental data [15,18,19] have shown its isovector components to be too weak. This weakness may not be surprising since the asymmetry term of the JLM OMP is obtained by differentiating a symmetric NM BHF calculation with respect to the asymmetry parameter. Full calculations of the BHF asymmetric NM have since been performed [20]. However, to correct shortcomings in our previous analyses [5], we present a new energy-dependent parametrization of the nucleon-nucleus OMP potential depths that is Lane consistent and features energy-dependent enhancements of the original isovector components [11]. These parametrizations are optimized by comparison between SM OMP predictions and measurements of nucleon elastic and quasielastic scattering and of reaction observables. Again this optimization process defines a new Lane-consistent, SM OMP that uses the NM OMP density dependence of JLM, and separate phenomenologically tuned energy dependencies for the isoscalar and isovector OMP components. This approach of a SM OMP guided by theory is similar in spirit to that used in Refs. [21,22]. As in our earlier works [5,14–16], the input point proton and neutron radial densities were obtained from Hartree-Fock-Bogoliubov (HFB) calculations performed using the finite-range, density-dependent Gogny force.

This paper is organized as follows. In Sec. II, Lane consistency is defined and some notation established. Section III details the Lane-consistent parametrizations of potential depth normalizations, as well as specifying the method used to obtain them. In Sec. IV comparisons between our new SM OMP predictions and elastic scattering, quasielastic (QE) scattering to isobaric analog states (IAS), and reaction observables are given. These comparisons are performed for over 30 nuclei identified in Table I, and in Tables 5 and 6 of Ref. [5], so that our SM OMP covers a broad range of masses from $A=40$ to $A=209$. Then in Sec. V we discuss the choice of an asymmetry parameter prescription, the uncertainties in the energy-dependent potential depth normalizations, and the sensitivity to the nuclear structure information contained in the point proton and neutron radial densities. We also compare our results with those found using other approaches.

II. LANE MODEL

In the Lane model [17], which assumes isospin symmetry in nuclei, the nucleon-nucleus OMP can be decomposed into isoscalar and isovector parts

$$U = U_0 + 4\frac{\vec{t}\cdot\vec{T}}{A}U_1, \tag{1}$$

where $\vec{t}$ and $\vec{T}$ are the isospins of the projectile and target nucleus, respectively, and A is the mass of the nucleus. The diagonal part of U in $(\vec{t},\vec{T})$ space represents the influence of the isovector potential on elastic scattering, whereas the off-diagonal t_+T_- part represents the quasielastic (p,n) transition between the ground state and its associated isobaric analog state. The central potential seen by a scattered neutron (proton) then has the form

$$U_{el}=U_0\pm\frac{1}{2}\frac{T_0}{A}U_1, \tag{2}$$

with $T_0=(N-Z)/2$, and the (p,n) transition potential reads

$$U_{QE}=\frac{1}{2}\frac{(0.5T_0)^{1/2}}{A}U_1. \tag{3}$$

Note that, although the elastic scattering potential is dominated by the isoscalar OMP components, the QE (p,n) transition is only sensitive to the asymmetry term of the OMP. Thus, to ascertain the quality of a Lane-consistent OMP, the proton and neutron elastic, and (p,n) processes must be analyzed simultaneously [23].

To be consistent with the notations of Refs. [10,11] and [5], which use

$$U_{el}=U_0\pm\alpha\tilde{U}_1, \tag{4}$$

we define $\tilde{U}_1=\frac{1}{4}U_1$ and $\alpha=(N-Z)/A$. Equation (3) then transforms into

$$U_{QE}=2\left(\frac{\alpha}{A}\right)^{1/2}\tilde{U}_1. \tag{5}$$

III. LANE-CONSISTENT SEMIMICROSCOPIC OMP

A. Lane-consistent formulation

In Ref. [5] we optimized the energy variations of the potential depth normalization factors $\lambda_V(E)$ and $\lambda_W(E)$, which are, respectively, the real and imaginary central potential components, separately for proton and neutron projectiles. By so doing, the isoscalar (or isovector) components of the OMP have different potential depths depending on the isospin of the projectile. Clearly that is not a Lane-consistent way of specifying the OMP.

In this paper, the optimization process is repeated, but Lane consistency is imposed on the OMP so that the same energy-dependent potential depth normalization factors can be used not only for the separate neutron and proton elastic scattering, but also for quasielastic (p,n) scattering. For elastic neutron (proton) scattering, it is convenient to use the central nuclear component of the OMP in nuclear matter of a given density $\rho=\rho_n+\rho_p$ and asymmetry $\alpha=(\rho_n-\rho_p)/\rho$, and which has the form

$$\begin{aligned}U_{el}(E)=&\lambda_V(E)[V_0(\tilde{E})\pm\lambda_{V1}(E)\alpha V_1(\tilde{E})]\\&+i\lambda_W(E)[W_0(\tilde{E})\pm\lambda_{W1}(E)\alpha W_1(\tilde{E})],\end{aligned} \tag{6}$$

where E is the incident projectile energy and $\tilde{E}=E-V_c$ is that energy shifted by the Coulomb potential V_c (for incoming protons only). λ_V, λ_W, λ_{V1}, and λ_{W1} are the real, imaginary, real isovector, and imaginary isovector potential depth normalization factors, respectively. In Eq. (6), the $V_0(\rho,E)$, $V_1(\rho,E)$, $W_0(\rho,E)$, and $W_1(\rho,E)$ quantities are calculated as shown in Sec. II of Ref. [5]. Note that for isovector parts of the potential, there are two normalization factors $\lambda_{V(W)}$ and $\lambda_{V1(W1)}$. So choosing facilitates the generalization of the present spherical SM OMP to deformed nuclei, for which only the λ_W factor should change significantly because of open channels that would be taken into account explicitly in coupled-channel calculations. To use the approach with finite nuclei, the ILDA [see Eqs. (24) and (27) of Ref. [5] which give the ILDA evaluated at the target position] has been applied to the NM OMP, folding it with realistic radial nuclear densities, and obtaining $U_{el}(r,E)$. As in Ref. [5], we use nuclear densities calculated in the HFB framework [24] with the Gogny D1S effective interaction [25]. With these, reliable predictions of experimental charge and matter distributions [24,26,27] have been found and they were used successfully in our earlier semimicroscopic OMP calculations [5,14–16].

The nuclear central OMP, $U_{el}(r,E)$, along with the spin-orbit (SO) potential given in Ref. [5], is then introduced in the Schrödinger equation for elastic scattering of a nucleon. This equation includes relativistic kinematics [28] and is solved using the ECIS [29] code, producing elastic differential cross sections $(d\sigma/d\Omega)$, analyzing powers (A_y), spin rotation observables, reaction cross sections (σ_R), and total cross sections (σ_T for incident neutrons only), which can be compared with experimental data.

The potential for a QE (p,n) transition, derived from Eqs. (4), (5), and (6), is

$$\begin{aligned}U_{QE}(r,E)=&2\left(\frac{\alpha(r)}{A}\right)^{1/2}[\lambda_V(E)\lambda_{V1}(E)V_1(r,E)\\&+i\lambda_W(E)\lambda_{W1}(E)W_1(r,E)].\end{aligned} \tag{7}$$

Again, for scattering from a finite nucleus, $V_0(r,E)$, $V_1(r,E)$, $W_0(r,E)$, and $W_1(r,E)$ are obtained by applying the ILDA (using HFB-Gogny nuclear densities) to their nuclear matter counterparts $V_0(\rho,E)$, $V_1(\rho,E)$, $W_0(\rho,E)$, and $W_1(\rho,E)$. For QE scattering the *local* form of the asymmetry parameter $(\alpha(r)=[\rho_n(r)-\rho_p(r)]/\rho(r))$ is used, and not its *average* form $[\alpha=(N-Z)/A]$. Note that using the local form might lead to numerical problems in the evaluation of the square root in Eq. (7) whenever locally $\rho_p>\rho_n$. In this case the average form of the asymmetry parameter is used. Section V A discusses the implications of the choice of a prescription for evaluating α.

If E is the energy of the incoming proton then U_{QE} is evaluated at $E+Q/2$, with Q as the Q value of the (p,n) IAS reaction. In this work, when experimental values of Q were not available, the Anderson formula [30] has been used. The (p,n) IAS transition potential is then placed in our distorted-wave Born approximation (DWBA) calculations, where the entrance and exit distorted waves were calculated using Eq.

TABLE I. Experimental QE (p,n) scattering database. Horizontal separations correspond to the data displayed in Figs. 5, 6, 7, and 9.

Projectile energy	Targets	Reference
22.8 MeV	^{56}Fe, ^{64}Ni, ^{70}Zn, ^{90,96}Zr, ^{117}Sn, ^{208}Pb	[33]
22.8 MeV	^{56}Fe	[34]
22.8 MeV	^{54,56}Fe, ^{58,61,62,,64}Ni, ^{90,96}Zr, ^{96}Mo, ^{96}Ru, ^{115}In, $^{117-120}$Sn	[35]
22.8 MeV	^{112,116,124}Sn	[36]
25.8 MeV	^{208}Pb	[37]
26.0 MeV	^{92}Mo	[38]
26.0 MeV	^{104}Pd	[39]
26.0 MeV	^{138}Ba, ^{142}Nd, ^{144}Sm	[40]
30.2 MeV	^{54,56}Fe, ^{93}Nb, ^{120}Sn, ^{208}Pb	[41]
35.0 MeV	^{56}Fe, ^{58}Ni	[42]
35.3 MeV	^{112}Sn, ^{116}Sn, ^{124}Sn	[43]
25.0, 35.0, 45.0 MeV	^{48}Ca, ^{90}Zr, ^{120}Sn, ^{208}Pb	[44]
120.0 MeV	^{90}Zr	[45]
134.0 MeV	^{48}Ca	[46]
135.0 MeV	^{54}Fe, ^{208}Pb	[47]
134.0, 160.0 MeV	^{48}Ca	[48]
160.0 MeV	^{90}Zr	[49]
200.0 MeV	^{90}Zr	[50]

(6) at $\tilde{E}$ and $E+Q$ for incident protons and neutrons respectively, as suggested in Ref. [31]. The SO part of the (p,n) transition potential is given by the isovector component of the Scheerbaum [32] SO form factor adjusted by the energy-dependent potential depth normalizations factors given in Sec V C of Ref. [5] and calculated at $E+Q/2$. The entrance and exit channel SO potential components were calculated at E and $E+Q$, respectively.

B. Search procedure

The optimization procedure consisted of several passes in which the global (λ_V and λ_W) and isovector (λ_{V1} and λ_{W1}) normalizations factors were improved alternatively. The first steps were to use OMPs defined by Eq. (6) to reproduce proton and neutron elastic scattering differential cross sections. The results give good first estimates of the isoscalar parts of the OMP and they are the essential parts of the elastic scattering potentials used in building the distorted wave functions for the DWBA approach of the QE (p,n) scattering. Reasonable estimates of the isovector parts of the OMP are obtained in these steps also. After stabilization of the λ factors, (p,n) scattering observables were included in the procedure, yielding small adjustments of the global factors (λ_V and λ_W) and more precise energy dependence of the isovector factors (λ_{V1} and λ_{W1}). This procedure was first performed in the $20 \leqslant E \leqslant 50$ MeV energy region (shaded zone in Fig. 1) where proton and neutron elastic and (p,n) experimental data were available for nearly the same incident energies. There are not much (p,n) data below 20 MeV due to the negative Q of the (p,n) IAS reaction, and not much proton elastic data are available below 10 MeV. Conversely, neutron elastic scattering data are very scarce above 50–70 MeV. Thus, the complete Lane consistency of our model [compliance with Eq. (6) for both proton and neutron elastic scattering, as well as with Eq. (7) for (p,n) QE scattering] can only be challenged with experimental data in the 20–50 MeV range, which constitutes the energy range of maximum confidence of our study. For the subsequent passes of the optimization process, we chose smooth functional forms for the energy-dependent normalization factors, and added $\sigma_T(E)$ and $\sigma_R(E)$ observables to the original data set. In that way we extend the range of this study from 1 keV to 200 MeV. After several cycles (including changes to the initial function forms) the search has converged and we obtained the parametrizations of the energy-dependent potential depth normalization factors λ_V, λ_W, λ_{V1}, and λ_{W1} given next. For completeness, the elastic scattering and reaction data we have used is the set detailed in Sec. IV A of Ref. [5], while the data on QE (p,n) scattering that we have used are listed in Table I.

C. Parametrizations of λ_V, λ_W, λ_{V1}, and λ_{W1}

As a result of the above optimization process, we get parametrizations of the energy-dependent potential depth normalizations. The functional forms were chosen only to reflect the energy variations of the normalization factors and not according to any specific physical consideration. Those parametrizations are displayed as curves in Fig. 1.

For the global (λ_V and λ_W) factors the functional forms adopted are similar to those found in Ref. [5]. The normalization of the real global potential depth λ_V which accounts for the data set we have used is given by

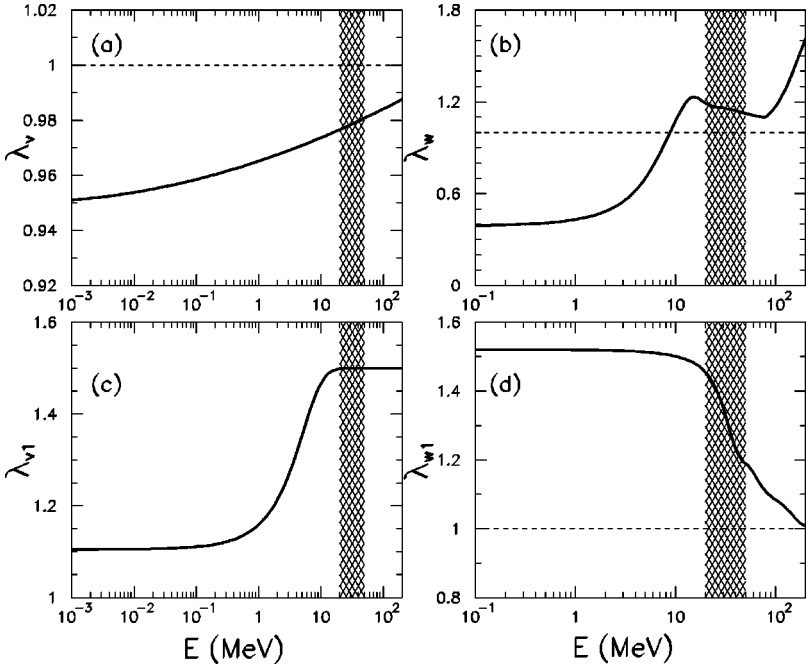

FIG. 1. Energy-dependent potential depths normalization factors λ_V, λ_W, λ_{V1}, and λ_{W1}, respectively, for (a) the overall real, (b) overall imaginary, (c) real isovector, and (d) imaginary isovector components of our semimicroscopic OMP. The hatched zones represent the energy range where the Lane consistency of the OMP can be thoroughly tested by comparison with proton and neutron elastic and QE (p,n) experimental data.

$$\lambda_V(E) = 0.951 + 0.0008 \ln(1000E) + 0.00018[\ln(1000E)]^2. \tag{8}$$

Above 1 MeV, this formulation produces normalizations that are close to those in Eq. (36) of Ref. [5], but they differ significantly below 1 MeV. Note, however, that the previous OMP [5] was not thoroughly tested at low energies. Between 1 keV and 200 MeV, λ_V varies between 0.95 and 0.99, exhibiting a nearly flat behavior over more than five decades.

The optimal normalization of the imaginary potential depth, λ_W, was found to follow

$$\lambda_W(E) = [1.24 - [1 + e^{[(E-4.5)/2.9]}]^{-1}] \times [1 + 0.06e^{-[(E-14)/3.7]^2}][1 - 0.09e^{-[(E-80)/78]^2}] \times \left[1 + \left(\frac{E-80}{400}\right)\Theta(E-80)\right], \tag{9}$$

where $\Theta(x)$ is the Heaviside step function. The functional form of Eq. (9) is identical to that of Eq. (39) in Ref. [5], but some parameter values have changed significantly. The biggest difference lies in the low energy region where the present strength of λ_W is larger than that given previously [5], improving the accuracy of the present OMP predictions over those found before [5] below 1 MeV.

The enhancement factor of the real isovector part of the OMP, λ_{V1}, is taken as

$$\lambda_{V1}(E) = 1.5 - 0.65[1 + e^{(E-1.3)/3}]^{-1}, \tag{10}$$

and the enhancement factor for the imaginary isovector OMP, λ_{W1}, as

$$\lambda_{W1}(E) = [1.1 + 0.44[1 + (e^{(E-40)/50.9})^4]^{-1}] \times [1 - 0.065e^{-[(E-40)/13]^2}] \times [1 - 0.083e^{-[(E-200)/80]^2}]. \tag{11}$$

In Fig. 1(c), $\lambda_{V1}(E)$ is shown to vary smoothly from 1.1 below 1 MeV to 1.5 above 10 MeV. Note that $\lambda_{V1}(E)$ is always significantly larger than 1.0. Here $\lambda_{W1}(E)$ [displayed in Fig. 1(d)] exhibits a plateau near 1.5 below 10 MeV and decreases to 1.0 at 200 MeV. In the 20–50 MeV region, where enough data are available to test completely for Lane consistency, $\lambda_{W1}(E)$ decreases from nearly 1.5 to 1.2. The energy variations of $\lambda_{V1}(E)$ and $\lambda_{W1}(E)$ outside the 20–50 MeV range (represented as hatched zones on Fig. 1) are not as thoroughly tested as in the region of maximum confidence, but still reflect the optimization of isovector potential depth with respect to elastic scattering and reaction data.

Finally, the values of the real and imaginary Gaussian ranges t_r and t_i used in the ILDA [Eqs. (24) and (27) of Ref. [5]] were varied to get a unique set of ranges for proton and neutron elastic scattering, reaction, and QE (p,n) scattering. As found before [5], the total (σ_T) and reaction (σ_R) cross sections are most sensitive to variations of t_r and t_i. The best compromises on the ILDA ranges we find are $t_r = 1.25$ fm and $t_i = 1.35$ fm. However, we stress that this choice is a global compromise and that different values of the ranges can be found to produce better agreement with the data in selected cases.

IV. RESULTS

A. Summary of the calculation process

For the sake of clarity, we briefly summarize the details of the calculations that produce the predictions for comparison with experimental data. For elastic scattering, the calculation

scheme is almost the same as that described in Sec. VI of Ref. [5]. The only differences are the presence of additional enhancement factors $\lambda_{V1}(E)$ and $\lambda_{W1}(E)$ for the isovector OMP components in Eq. (6) and our use of the modified expressions (8) and (9) for the global potential depths normalizations $\lambda_V(E)$ and $\lambda_W(E)$. Moreover, for the present OMP, the energy range of validity spans 1 keV to 200 MeV. For QE (p,n) scattering, the (p,n) transition potential, defined by Eq. (7) and calculated at $E+Q/2$, has been used in the DWBA framework. The (proton) entrance channel distorted wave was calculated at energy $\tilde{E}$ and the (neutron) exit channel wave at $E+Q$. Unless otherwise stated, the results of all calculations shown in this work were performed using the above schemes.

B. Elastic proton and neutron scattering, and reaction

Herein we show that the current semimicroscopic OMP is at least as good as that established in Ref. [5] for all of the elastic scattering and reaction observables. In Fig. 2 we display the results of $\vec{p}+{}^{58}$Ni elastic scattering calculations using the present Lane-consistent semimicroscopic OMP. They are compared with experimental data for differential cross sections and analyzing powers. These results compare well also to those given in Fig. 21 of Ref. [5]. Indeed, the results from the present work are nearly indistinguishable from those found previously [5], both producing good descriptions of $\vec{p}+{}^{58}$Ni scattering up to 200 MeV.

In Fig. 3 the results of $\vec{n}+{}^{208}$Pb scattering calculations (including a Coulomb spin-orbit potential [51]) are compared with experimental data. Again, comparison with the corresponding results given in Fig. 15 of Ref. [5] reveals that both the present OMP and its predecessor account for the experimental data very well. The predictions are very similar to one another. But in Fig. 3 we now display differential cross sections measured at 55, 65, and 75 MeV [52] that were not available during the optimization process. This illustrates that our OMP does predict measurables well. Finally, in Fig. 4 we compare the results of our OMP calculations with experimental total cross sections between 1 keV and 200 MeV for typical nuclei. The comparison with experimental data above 1 MeV is very similar to that given in Fig. 9 of Ref. [5]. Overall the agreement is very good, with discrepancies of at most 10%. Below 1 MeV, discrepancies are more sizable, yet the overall shape of the total cross sections is accounted for reasonably well. Calculations of proton and neutron scattering and of reaction observables on the many spherical and near-spherical nuclei considered previously [5] also gave comparable results, showing that the present Lane-consistent semimicroscopic OMP performs at least as well as its non-Lane-consistent predecessor [5] on the same set of observables.

C. Quasielastic (p,n) scattering

The QE (p,n) scattering constitutes a strong test of the isovector component of the OMP since only the $V_1(r,E)$ and $W_1(r,E)$ components appear in the central (p,n) transition potential, Eq. (7). That is evident in Fig. 5 in which we show our predictions of QE (p,n) scattering differential cross sections and analyzing powers compared with measured ones for 18 nuclei and at energies near 23 MeV. The predicted QE cross sections, displayed in Figs. 5(a) and 5(b), match both the shape and amplitude of experimental data for all isotopes. But in detail, we note that, while the forward angle data are well reproduced by our OMP results, mid- and/or back-angle QE scattering cross sections sometimes are underestimated. That is especially so with ^{112}Sn, ^{115}In, and ^{124}Sn. However, coupling to the analog-excited levels (not included in the present DWBA approach) can be expected to lower the calculated mid- to back-angle differential cross sections [53]. In Fig. 5(c), the calculated analyzing powers are compared with the experimental data. The overall shapes, amplitudes, and phases are reproduced reasonably for angles $\theta \leqslant 70°$, but the details as well as the experimental data at backward scattering angles are not well accounted for by our calculations. That is also the case with the purely phenomenological analysis [33] of the same data.

In Fig. 6 we compare our calculated QE (p,n) differential cross sections with data at 26, 30, and 35 MeV for various target nuclei and clearly our semimicroscopic OMP accounts fairly well for the QE (p,n) reactions. As with the results given in Fig. 5, the agreement is not perfect. But the essential features of the experimental data are well described by the model. In Fig. 7 we compare predictions with data [44] taken from a wide range of target nuclei (from ^{48}Ca to ^{208}Pb) at proton energies of 25, 35, and 45 MeV. Clearly the energy dependence of the isovector component of our OMP is well described in our model, since the calculated angular distributions match the experimental data quite well. Again, the agreement is not perfect, but they are comparable to those found using a purely phenomenological approach [44]. Similar QE (p,n) calculations were performed for 49.4 MeV protons incident on ^{93}Nb, ^{120}Sn, and ^{208}Pb. The comparisons with data [41] are similar to those shown above and there are similar conclusions to be drawn.

The angle-integrated QE (p,n) IAS cross sections (σ_{QE}) also were calculated as functions of incident proton energy. In Fig. 8 the results are compared with data for the ^{208}Pb$(p,n)^{208}$Bi, ^{91}Zr$(p,n)^{91}$Nb, and ^{92}Mo$(p,n)^{92}$Tc reactions. For ^{208}Pb [Fig. 8(a)], the agreement is very good from 25 to 50 MeV. In the case of ^{91}Zr [Fig. 8(b)], the calculation seems to overestimate the data; however, the most recent data set [54] (shown as triangles) agrees better with our calculation, perhaps hinting that older data values are too low. Moreover, looking back at Fig. 7(b) it does not seem to indicate that the calculated angle-integrated cross sections overestimate the experimental ones at 25, 35, and 45 MeV for the even-even ^{90}Zr core. Finally, in Fig. 8(c) we show the integrated (p,n) IAS cross section for the neighboring ^{92}Mo nucleus. The results are in good agreement with experimental data in the 18–26 MeV range.

In Fig. 9 we present a comparison with data of our results for energies in excess of 100 MeV. In this energy regime, the Lane consistency of our model could not be tested completely due to the scarcity of neutron elastic scattering data above 75 MeV. In Fig. 9(a), ^{48}Ca(p,n) QE scattering differential cross sections at 135 and 160 MeV are displayed. At

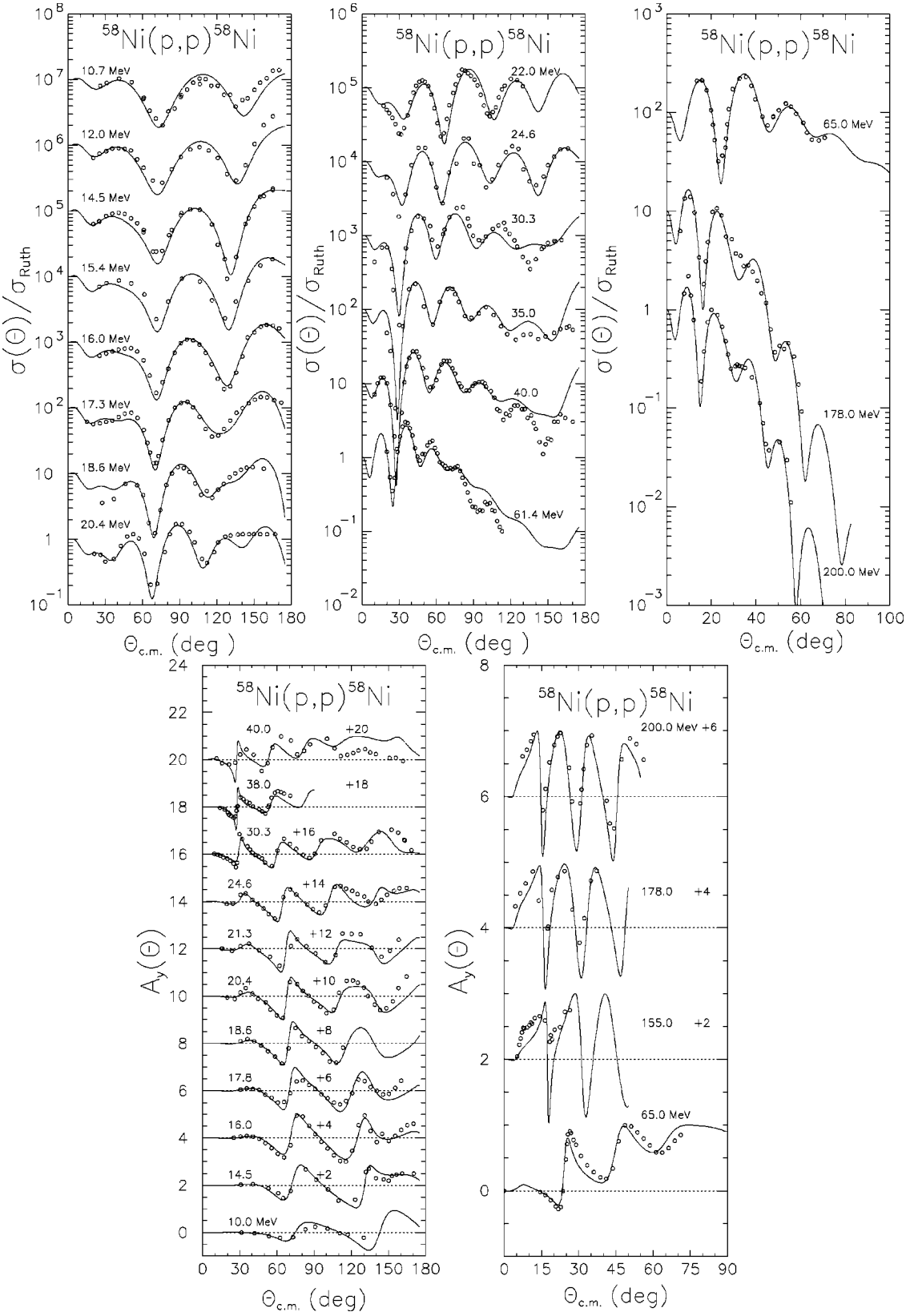

FIG. 2. Predicted scattering cross sections and analyzing powers (solid lines) compared with experimental data (open circles) for polarized protons incident on ^{58}Ni between 10 MeV and 200 MeV. Note that elastic cross sections are presented as ratio to Rutherford cross sections (σ_{Ruth}). These are offset by factors of 10, while analyzing powers are shifted by 2.

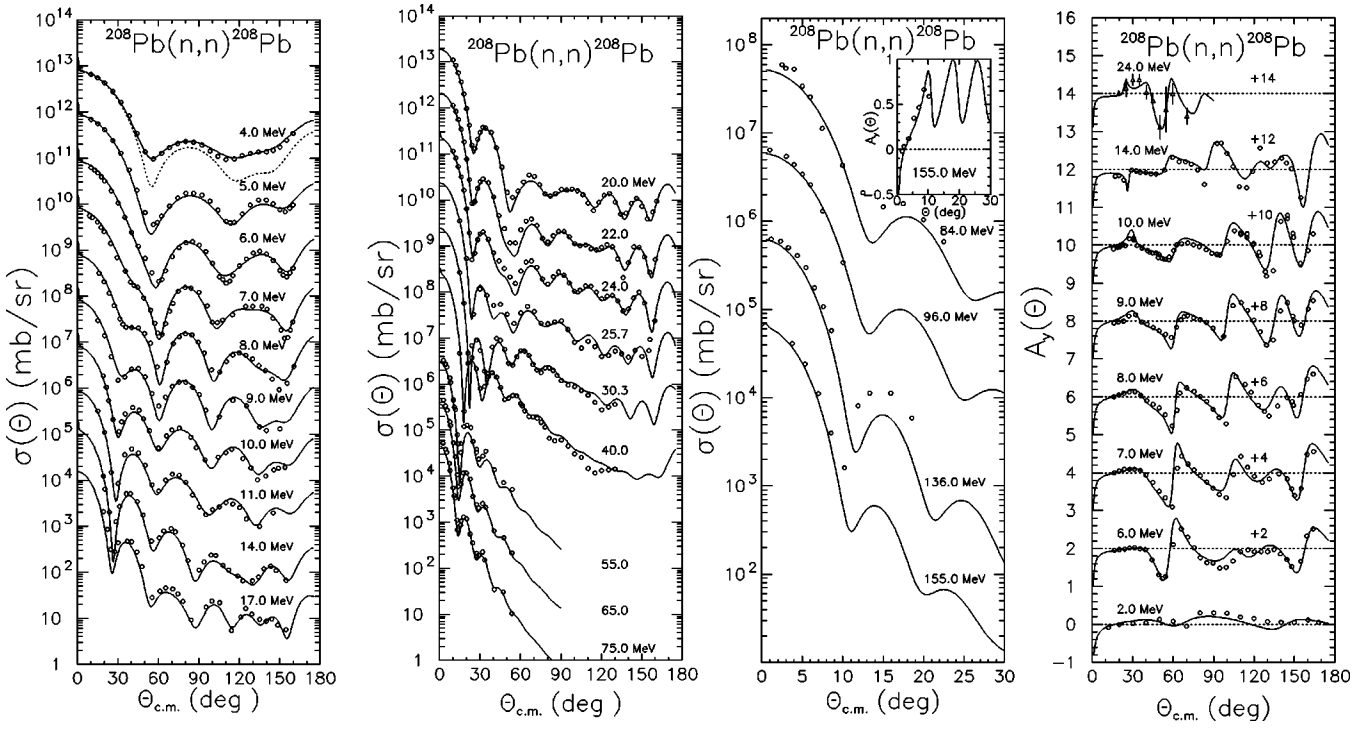

FIG. 3. Comparison of predicted differential cross sections and analyzing powers with experimental data, for polarized neutrons scattered from ^{208}Pb between 2 and 155 MeV. Note that the differential cross sections are offset by factors of 10, while analyzing powers are shifted by 2. The solid lines represent the results of our calculations (including compound nucleus contributions) and dotted lines represent the direct interaction components of the differential cross section. The Coulomb SO potential is considered in this analysis.

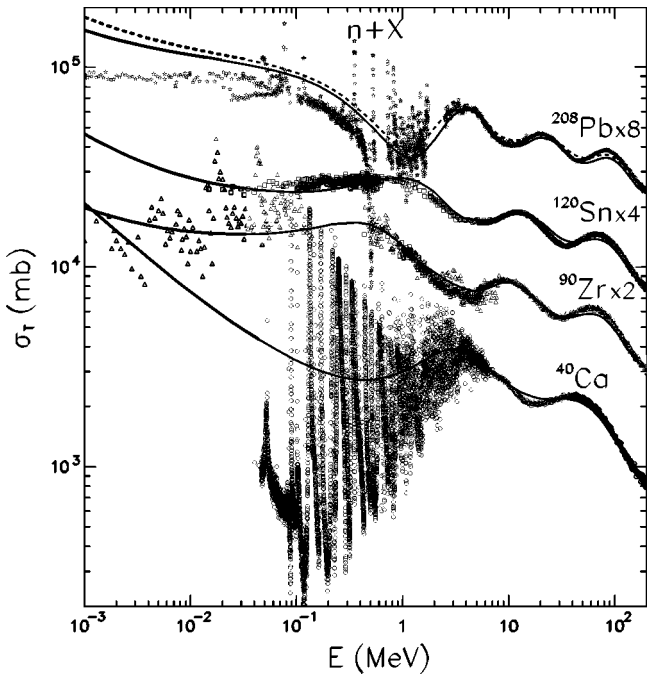

FIG. 4. Comparisons between calculated (solid lines) and experimental (symbols) total cross sections for neutrons incident on ^{40}Ca, ^{90}Zr, ^{120}Sn, and ^{208}Pb. The dashed line represents calculations performed using nuclear densities obtained though HF+RPA calculations for ^{208}Pb.

both energies the semimicroscopic OMP calculations overestimate the cross sections at forward scattering angles. For the QE ^{90}Zr(p,n) reaction at 120 MeV, the results of which are shown in Fig. 9(b), the data are well reproduced by our calculations, although at 160 and 200 MeV the predicted QE scattering peaks are too large and too narrow. Comparisons performed at 135 MeV for ^{54}Fe(p,n) and ^{208}Pb(p,n) QE scattering [Fig. 9(c)] also show that our OMP calculations tend to overestimate QE (p,n) scattering at the forward scattering angles. Moreover, the structure of calculated ^{208}Pb(p,n) differential cross section exhibits oscillations that are not evident in the experimental data. But there are only four such data points. In Fig. 9(d) the analyzing powers for QE (p,n) scattering from ^{48}Ca at 134 MeV and from ^{90}Zr at 160 MeV are shown. Given the sensitivity of such data, our results are quite good in comparison with observation.

Overall we believe that the potential depth normalization of our semimicroscopic OMP allows for a good, Lane-consistent description of elastic and quasielastic scattering and of reaction data where the Lane consistency is completely tested (i.e., from 20 to 50 MeV). For lower energy proton and neutron scattering and reaction data, our OMP also produces observables that closely match. At higher energies, while proton and neutron elastic scattering observables are well reproduced, QE (p,n) differential cross sections seem to be overestimated at forward scattering angles. However, other microscopic approaches [46–49] do not perform significantly better than does the present model at me-

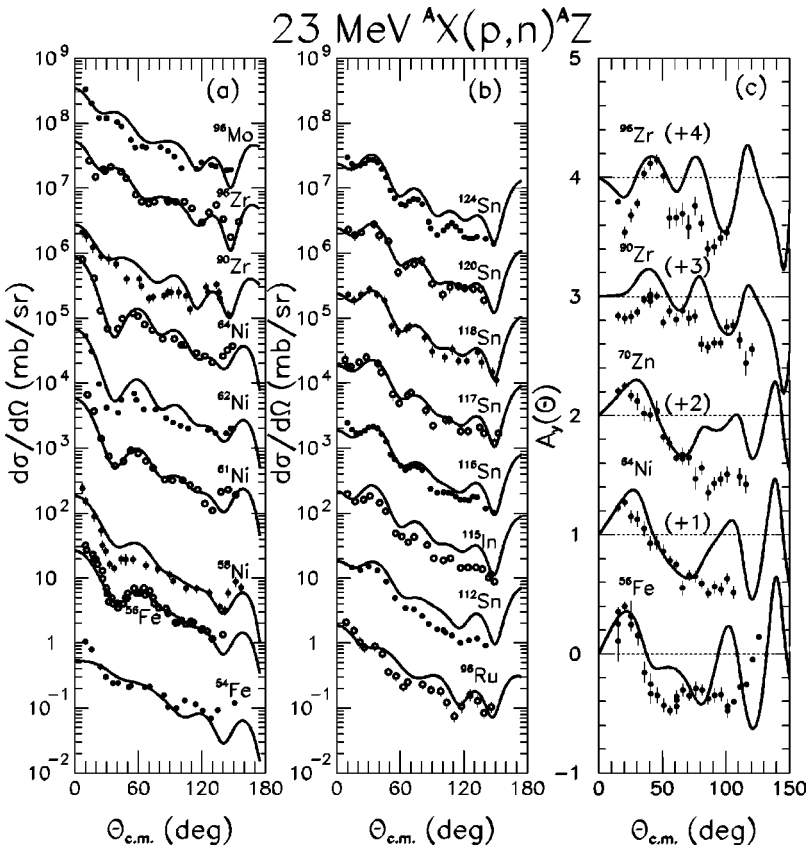

FIG. 5. Comparison between predicted (solid lines) and experimental (symbols) QE (p,n) differential cross sections (a), (b) and analyzing powers (c), for 23 MeV protons incident on ^{54}Fe, ^{56}Fe, ^{58}Ni, ^{61}Ni, ^{62}Ni, ^{64}Ni, ^{70}Zn, ^{90}Zr, ^{96}Zr, ^{96}Mo, ^{96}Ru, ^{112}Sn, ^{115}In, ^{116}Sn, ^{117}Sn, ^{118}Sn, ^{120}Sn, and ^{124}Sn. Note that the differential cross sections are offset by powers of 10, while analyzing powers are shifted by increments of 1.

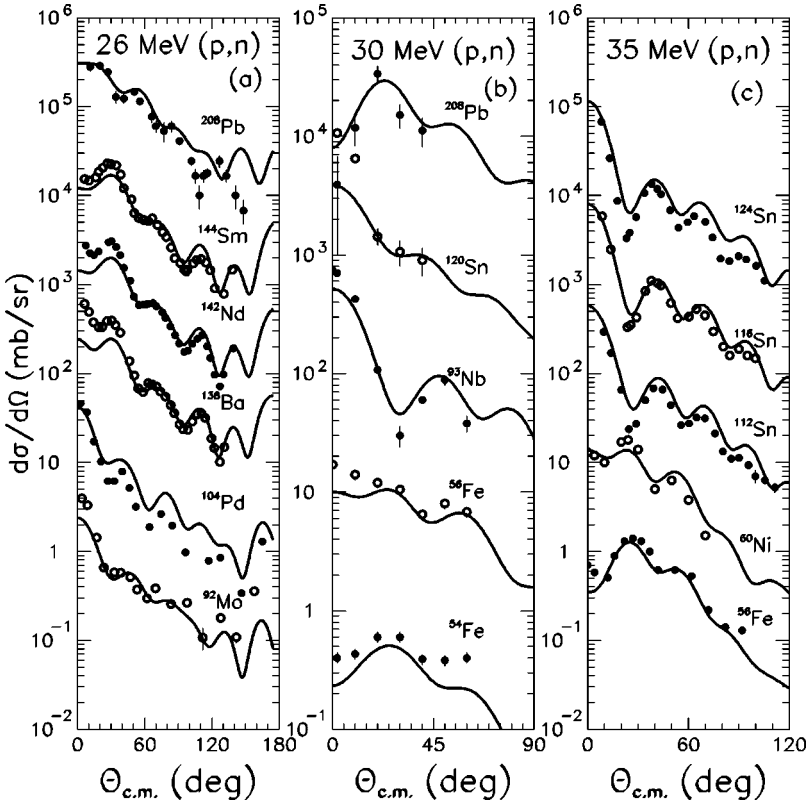

FIG. 6. Comparison between predicted (solid lines) and experimental (symbols) QE (p,n) differential cross sections for 26 MeV (a), 30 MeV (b), and 35 MeV (c) protons incident on ^{54}Fe, ^{56}Fe, ^{60}Ni, ^{92}Mo, ^{93}Nb, ^{104}Pd, ^{112}Sn, ^{116}Sn, ^{120}Sn, ^{124}Sn, ^{138}Ba, ^{142}Nd, ^{144}Sm, and ^{208}Pb. Note that the differential cross sections are offset by powers of 10.

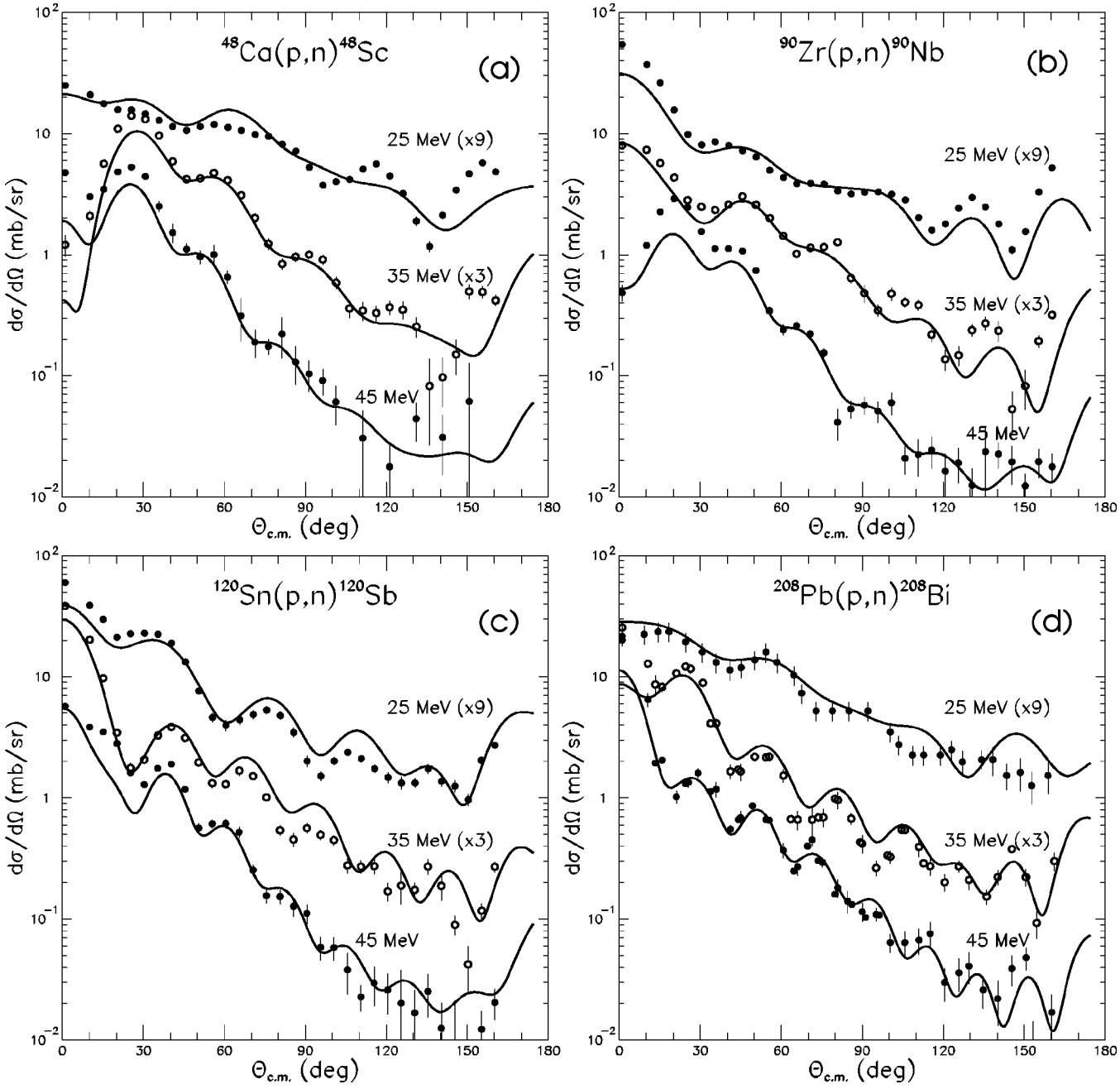

FIG. 7. Comparison between predicted (solid lines) and experimental (symbols) QE (p,n) differential cross sections for 25 MeV, 35 MeV, and 45 MeV protons incident on ^{48}Ca (a), ^{90}Zr (b), ^{120}Sn (c), and ^{208}Pb (d). Note that the differential cross sections are offset by powers of 3.

dium energy. Moreover, the differences between our predictions and medium energy data should not be overemphasized as the adjustments of $\lambda_{V1}(E)$ and $\lambda_{W1}(E)$ that would be needed to make calculated observables match experiment are well within the estimation of the uncertainties on potential depth normalization factors as we discuss in the next section.

V. DISCUSSION

A. Choice of a prescription for the asymmetry parameter

First, we discuss the physical implications of the choices that were made and described in Sec. III. Taking the local asymmetry parameter as $\alpha(r)=(\rho_n-\rho_p)/(\rho_n+\rho_p)$ for both the elastic scattering and the QE (p,n) transition potential can be interpreted as the evaluation of the asymmetry term of the OMP in nuclear matter *before* proceeding with finite nuclei through ILDA. Conversely, the choice of using the average $[\alpha=(N-Z/A)]$ asymmetry parameter corresponds to the case where α is directly calculated for a finite nucleus with a given value of isospin T_0. However, as noted earlier, the local prescription for the asymmetry parameter can lead to an indeterminate form when locally $\rho_p>\rho_n$. Here ^{54}Fe proved to be an example. In that case the $\alpha=(N-Z)/A$ prescription for the asymmetry parameter was used.

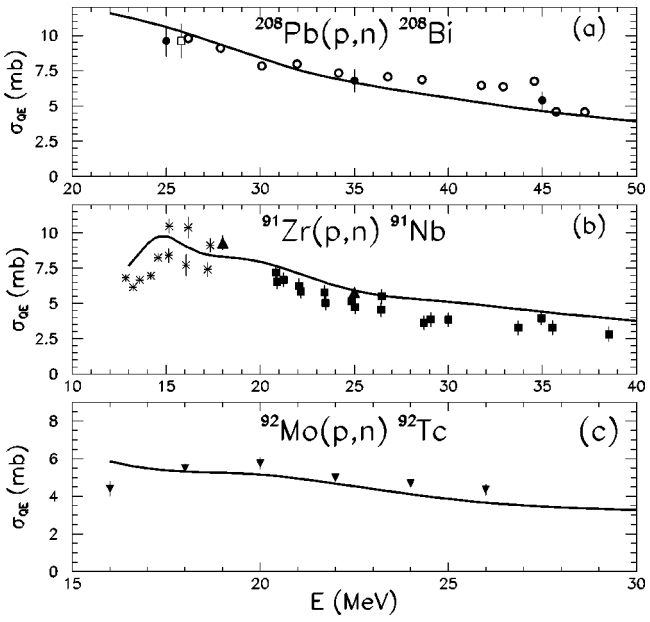

FIG. 8. Comparison between predicted (solid lines) and experimental (symbols) QE (p,n) angle-integrated cross sections, for ^{208}Pb (a), ^{91}Zr (b), and ^{92}Mo targets. Open circles, open square, solid circles, stars, up triangles, solid squares, and down triangles represent data from [55] (corrected as in [56]), [37], [44], [57], [54], [55], and [58], respectively.

To appraise the effect of using these prescriptions, we show, in Fig. 10, QE (p,n) scattering observables calculated using the local (solid line) and average (dashed line) prescriptions for the asymmetry parameter, for the case of 23 MeV polarized protons incident on ^{64}Ni. Evidently the prescription used to calculate the asymmetry parameter has a noticeable effect on the OMP and on the attendant predictions of observables. The two prescriptions also lead to integrated cross sections that differ noticeably (12% in the present case) and slightly different shapes. Nevertheless, both prescriptions do produce reasonable fits to the data, and our preference for the local asymmetry parameter prescription is motivated by the fact the local prescription takes into account more microscopic structure information, such as the difference between proton and neutron densities root mean square (rms) radii. Since the average prescription indeed assumes a simple scaling between proton and neutron density distributions, their rms radii are identical.

B. Uncertainties of potential depth normalization factors

In this section, we evaluate the range of the uncertainties associated with the potential depth normalization factors, λ_V, λ_W, λ_{V1}, and λ_{W1}, defined in Eqs. (8)–(11).

We will focus first on the energy range of maximum confidence, i.e., 20–50 MeV. In this region we estimate the uncertainty in λ_V's and λ_W's to be no more than 1.5% and 10%, respectively. This estimate is obtained by comparing the values given from Eqs. (8) and (9) to those inferred from best fits to individual angular distributions. For the isovector normalization factors λ_{V1} and λ_{W1}, the uncertainties are estimated to be of the order of 10%. To obtain this value we have performed QE (p,n) calculations for ^{208}Pb using not only the mean-field HF/D1S calculated densities but also the correlated densities obtained through HF+RPA calculations [59], the latter again made using the Gogny effective interaction. Note that, since ^{208}Pb is a doubly closed shell nucleus in which no pairing is present, the HF and HFB solutions coincide. In the inset to Fig. 11, the predicted charge and point neutron density distributions are shown as dashed (HF) and dotted [random phae approximation (RPA)] curves. They are compared with those extracted from measurements [60,61]. The RPA densities describe the structure data better, but their use alters noticeably the amplitude of the QE differential cross section prediction as is shown in the body of Fig. 11. To get a better agreement for the (p,n) predictions when using the RPA densities, λ_{V1} and λ_{W1} would have to be changed by about 10%. The effect of using RPA densities instead of HF densities on the calculations of $n+^{208}$Pb total cross section is illustrated in Fig. 4 (dashed curves). But the differences seen in Fig. 4 can be taken into account also by changes of the potential depth normalizations within their respective uncertainties. The 10% uncertainty on the isovector components is viewed as a measure of the effect of changing from a ''good'' description of the nuclear structure of ^{208}Pb (HF calculation) to a ''better'' one (RPA calculation) [59], and is adopted as our estimate of the uncertainties on the isovector normalization factors.

Moving away from the 20–50 MeV energy range of maximum confidence increases the uncertainties as might be expected. We estimate that outside this range the above uncertainties should be multiplied by a factor of 1.5–2.0. Finally, we stress the existence of correlations between the different potential depth normalization factors. Those correlations, which result in part from the imposed Lane consistency in Eqs. (6) and (7), explain the 1.5–2.0 spread of the multiplicative factor for normalizations outside the 20–50 MeV region. If the Lane consistency is ignored, then good agreement with individual data sets can be obtained with the uncertainties in some normalization factors being twice as large, while the uncertainties in the remaining factors do not change. Conversely, by trying to maintain Lane consistency below 20 MeV and above 50 MeV, the uncertainties can be kept within 1.5 times their maximum confidence values if such changes are performed in a correlated way. Ideally, energy-dependent error matrices for the four normalization parameters defined by Eqs. (8)–(11), including the off-diagonal covariance information, should be presented. In practice, as a result of the uneven sampling of the energy and mass distributions in the experimental data set as well as to the presence of unknown systematic experimental uncertainties on those data, an automated search on the normalization factors is extremely difficult to perform without introducing biases. Therefore, only the $\times 2.0$–$\times 1.5$ (depending on how ''cleverly'' one changes the factors) augmentation of the normalization factor uncertainties is presented here.

C. Sensitivity to nuclear density distributions

In the preceding subsection, we discussed how experimental proton and neutron elastic and (p,n) scattering data

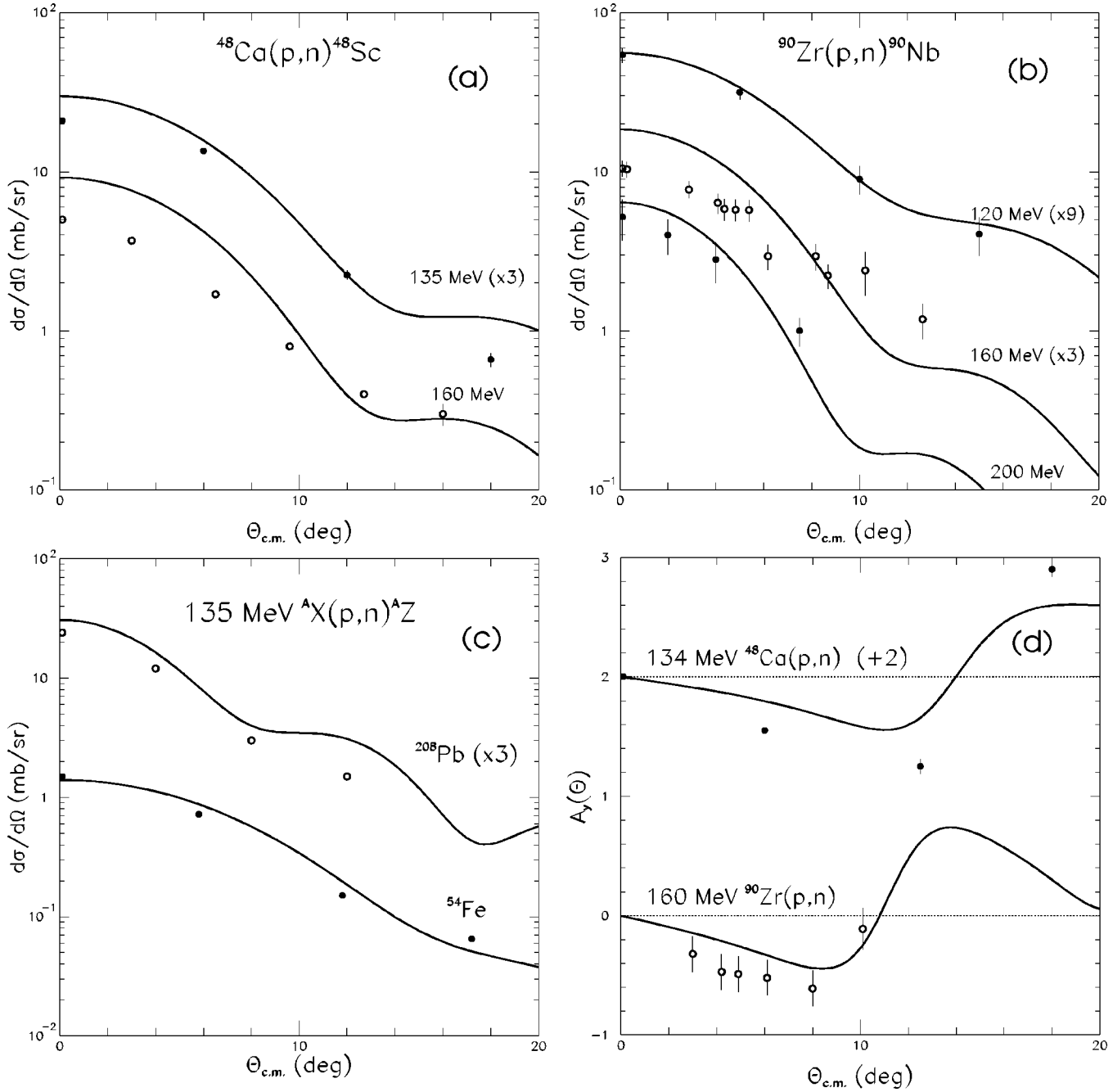

FIG. 9. Comparison between predicted (solid lines) and experimental (symbols) QE (p,n) differential cross sections (a), (b), and (c), and analyzing powers (d), for energies above 100 MeV. Note that the differential cross sections are offset by powers of 3, while analyzing powers are shifted by increments of 2.

can help narrowing the range of parameters used in our semimicroscopic OMP approach, the emphasis being on the parametrization of the complex, *N*-*N* effective interaction. Now we focus on the nuclear densities used in the OMP calculations and on what we may learn about them from comparisons between proton and neutron elastic and QE (p,n) scattering data and the semimicroscopic OMP predictions. More precisely, since proton density information is very well known from electron scattering experiments [26,27,60], QE (p,n) scattering by being essentially sensitive to the $\rho_n - \rho_p$ difference [36,37,40,62] indirectly should probe the neutron density distributions.

First we compare the nuclear density distributions calculated in the HFB framework with experimental observables. The inset in Fig. 11 displays experimental [60,61] and calculated charge and point neutron radial densities for ^{208}Pb. This figure shows that our HF and HF+RPA [24] calculations reproduce the charge and neutron radial density distributions well, yet the HF+RPA calculation exhibits better agreement with the data as is expected [59]. To further test the quality of these nuclear densities, calculated proton and neutron distributions rms radii are compared with their experimental counterparts [63] in Table II for some of the isotopes included in our experimental database. These compari-

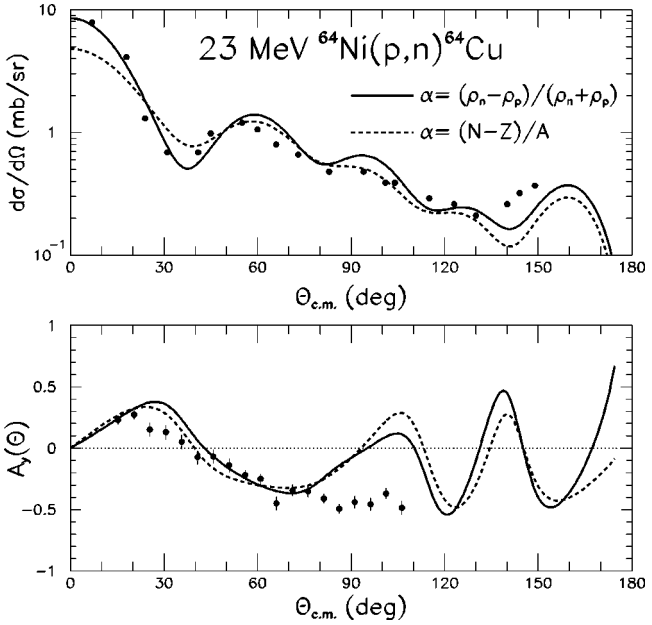

FIG. 10. Comparison between calculations using the local (solid line), average (dashed lines) prescriptions (see text) for the asymmetry parameter, and experimental data (symbols) for ^{64}Ni$(p,n)^{64}$Cu QE scattering at 23 MeV. The top panel displays differential cross section and the bottom panel displays analyzing power.

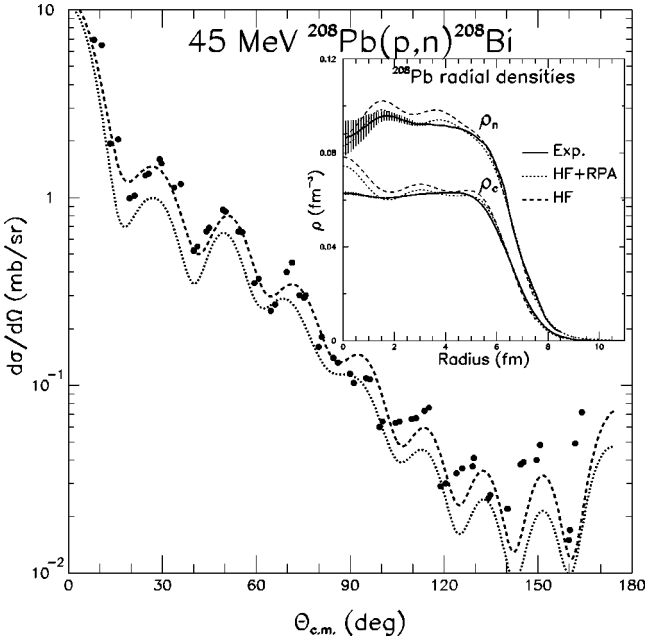

FIG. 11. Comparison between differential cross section calculations using HF nuclear densities (dashed lines), HF+RPA densities (dotted lines), and experimental data (symbols) for ^{208}Pb$(p,n)^{208}$Bi QE scattering at 45 MeV. The inset displays comparisons between calculated and experimental [60,61] point neutron and charge radial density distributions for ^{208}Pb.

TABLE II. Comparison between measurements [63] and present HFB and HF+RPA predictions for neutron, proton, and charge densities rms radii.

	$\langle r_n^2\rangle^{1/2}$ (fm)	$\langle r_p^2\rangle^{1/2}$ (fm)	$\langle r_{ch}^2\rangle^{1/2}$ (fm)
^{40}Ca expt.	3.491	3.392	3.482
^{40}Ca HF	3.368	3.412	3.470
^{48}Ca expt.	3.625	3.396	3.470
^{48}Ca HF	3.579	3.452	3.500
^{58}Ni expt.	3.700	3.686	3.772
^{58}Ni HFB	3.702	3.688	3.758
^{64}Ni expt.	3.912	3.745	3.845
^{64}Ni HFB	3.870	3.788	3.840
^{90}Zr expt.	4.289	4.204	4.280
^{90}Zr HFB	4.267	4.219	4.270
^{116}Sn expt.	4.692	4.546	4.619
^{116}Sn HFB	4.656	4.562	4.610
^{124}Sn expt.	4.851	4.599	4.670
^{124}Sn HFB	4.753	4.619	4.663
^{208}Pb expt.	5.593	5.453	5.503
^{208}Pb HF	5.576	5.442	5.482
^{208}Pb HF+RPA	5.653	5.465	5.515

sons show that the proton, neutron, and charge distributions rms radii over the whole range of studied nuclei are well defined by HFB calculations. Last, we note that the difference between neutron and proton rms radii for the Sn isotopes [64] also is well defined by the HFB calculations. Overall the HFB densities used as input to our SM OMP are in such remarkable agreement with the measured charge and neutron radial densities that the good agreement observed in Sec. IV between experimental and predicted elastic and quasielastic scattering cross sections is partially explained.

The next question is the sensitivity of our SM OMP to variations of these densities. We ask if our SM OMP calculations help discriminate between any available ''bad,'' ''good,'' and ''better'' descriptions of nuclear structure. Figures 4 and 11 provide some insight into this as they reveal the sensitivity of our SM OMP prediction to the density differences between HF and HF+RPA calculations. However, since these differences also can be accounted for by potential depth normalizations factors within our estimated uncertainties, assessing the respective merits of those two nuclear structure approaches using nucleon scattering information as the *only criterion* is obviously not within the capabilities of our approach. Nevertheless, the above example represents a worst case situation by discriminating between two already good descriptions of nuclear densities.

D. Comparisons with other OMPs

To check the consistency of our OMP with earlier approaches to the separation of central nucleon-nucleus OMPs

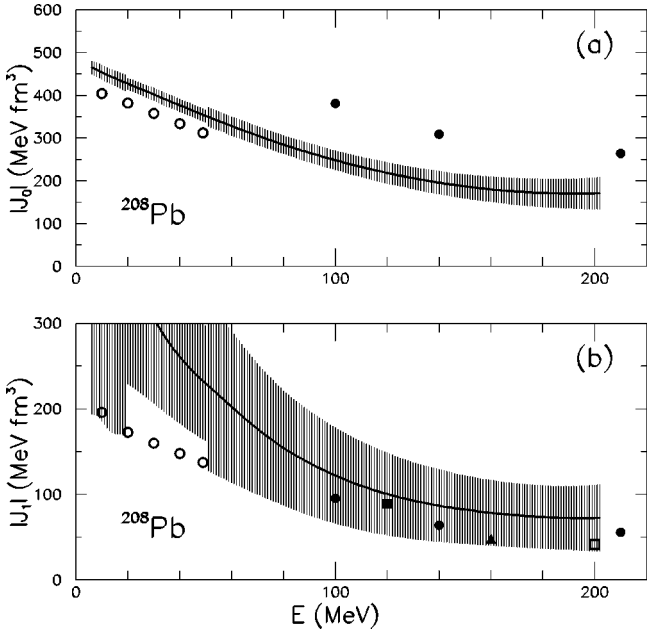

FIG. 12. Moduli of the isoscalar (a) and isovector (b) components of our semimicroscopic OMP (solid lines with shaded uncertainties ranges from Sec. V B) compared to those derived from other approaches [56,65–68]. See text for details.

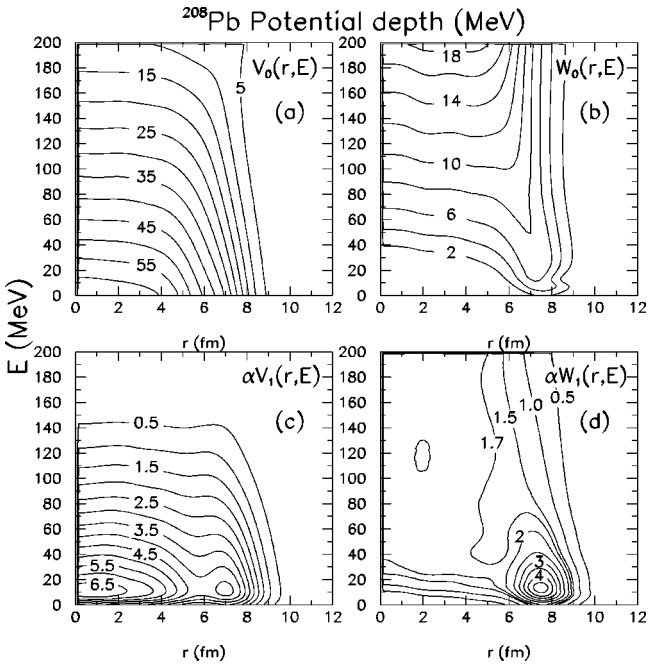

FIG. 13. Radial shape and energy dependence of the isoscalar and isovector OMP components for ^{208}Pb.

into isoscalar and isovector components we study the respective moduli $|J_0|$ and $|J_1|$ of the isoscalar and isovector components of our SM OMP. They are shown by solid lines in Fig. 12 with shaded uncertainty ranges as specified in Sec.V B. They are compared with OMP predictions [56,65] shown by the open and solid circles, respectively, for ^{208}Pb as the target. Moreover, isovector volume integrals extracted from forward angle ^{90}Zr(p,n) IAS cross sections measured at 120, 160, and 200 MeV are shown by the solid squares [66], the triangles [67], and the open squares [68], respectively. At 200 MeV, $|J_1|$ is extracted from the ^{90}Zr Fermi transition unit cross section of Fig. 29 of Ref. [68] using Eq. (2.20) of the same paper. We note that in the 120–200 MeV range, $|J_1|$ is nearly mass independent. We adopt the $|J_1|$ values obtained for ^{90}Zr because in heavy nuclei the IAS is located near the Gamov-Teller peak and therefore is difficult to resolve in (p,n) reactions at medium energies. For the isoscalar component, all three approaches, ours and those of Refs. [56,65], produce volume integrals that exhibit the same energy dependence. But differences of normalization are evident from Fig. 12(a). While these differences remain moderate (about 10%) between our approach and that of Ref. [56], larger differences exist between the results of our calculations and those of Ref. [65].

The isovector component of the OMP [shown in Fig. 12(b)] reveals other differences. While the high energy behavior of the isovector components [65–68] agrees well with our calculated values and estimated uncertainties, at low energy our SM OMP overestimates the isovector component specified elsewhere [56] and by a large amount (about 50% larger in fact). To reconcile these apparent contradictions one must remember that comparing volume integrals of OMPs is only meaningful when they have comparable radial shapes. The evolution of the radial shapes of our SM OMP for ^{208}Pb is displayed in Fig. 13 for the real isoscalar (a), imaginary isoscalar (b), real isovector (c), and imaginary isovector (d) components. Note that the real isovector component (c) is always much smaller than the real one (a). But in the vicinity of 20 MeV, the imaginary isoscalar (b) and isovector (d) components have comparable depths. This result leads us to reassess the validity of using the DWBA approximation for the present calculations. However, our tests have shown that calculating the QE (p,n) scattering in the coupled-channel framework instead of the DWBA approximation brings only negligible corrections to the (p,n) cross sections. Note also that the influence of isovector components weakens with increasing energy. Indeed the real isovector component nearly vanishes for energies in excess of 150 MeV and the imaginary isovector component is essentially flat between 100 and 200 MeV. In contrast, the imaginary isoscalar component grows in importance with increasing energy. Thus the isovector components of the OMP will have a weak influence on nucleon scattering between 150 and 200 MeV. Moreover and in agreement with other findings [69], at high energy $|J_1|$ is dominated by the imaginary isovector OMP component. A third point is that the disagreement between our low energy isovector volume integrals and those of Ref. [56] is most likely due to a very strong surface component present in the imaginary isovector component of our OMP.

Since the above comparisons do not allow us to be completely conclusive about the quality of our Lane-consistent OMP, we compare the nucleon mean free paths predicted in our approach with those from other work [20], wherein mean free paths have been calculated in asymmetric NM by using an extended Brückner-Hartree-Fock approach. The same quantities are calculated in our approach using the formula given in Ref. [20] and Eq. (6). The results are displayed in

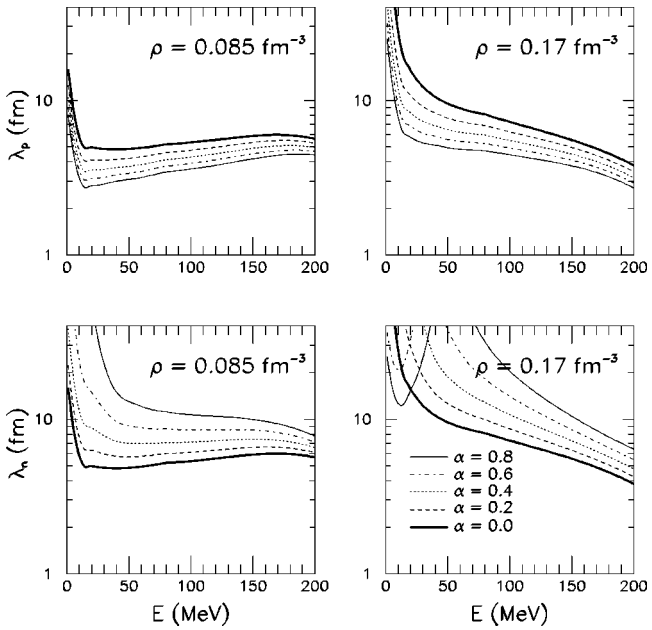

FIG. 14. Proton (top panels) and neutron (bottom panels) mean free paths calculated for densities of $\rho=0.085$ fm^{-3} (left panels) and $\rho=0.17$ fm^{-3} (right panels), and for asymmetry parameters α ranging from 0.0 to 0.8.

Fig. 14. Comparison of the mean free paths at nuclear surface density ($\rho=0.085$ fm^{-3}) shows that the symmetric NM mean free paths calculated using our SM OMP agree very well with those of Ref. [20]. But at the same density for high asymmetries ($\alpha>0.4$), our SM OMP predicts mean free paths that are noticeably different. However, within the range of asymmetries encountered between drip lines in finite nuclei ($\alpha\leqslant 0.4$), the mean free paths from our calculations and from Ref. [20] agree very well up to 150 MeV. It is not surprising that the two sets of calculations at high asymmetry disagree since the JLM approach [11], upon which our SM OMP is based, only uses first order perturbation expansion around symmetric NM to evaluate the asymmetry term of the NM potential whereas the extended BHF calculations [20] were made in asymmetric NM.

Our results calculated at the ''interior'' density ($\rho=0.17$ fm^{-3}) also can be compared with the BHF mean free paths [20]. At this density, the agreement between the two calculations, while fairly good at high energy, degrades with decreasing energies. At low energy the projectile does not penetrate the target deeply and thus mainly probes the surface of the potential. Conversely, at high energy the projectile probes more of the interior of the OMP. Thus the SM OMP parameters optimized at low energy mainly reflect effects of the NM OMP at ''surface'' densities while those optimized at high energies are more sensitive to the NM OMP at ''interior'' densities. Both features agree with the findings of Ref. [20]. The mean free paths shown in Fig. 14 can also be compared with other estimates [70,71]. Our calculations for $\alpha=0.2$ and $\rho=0.17$ fm^{-3} when compared to the ^{208}Pb proton mean free paths as calculated at $r=0$ fm (Fig. 10 of Ref. [70]) are in good agreement between 100 and 200 MeV.

E. Other remarks

The isovector term in the SO potential has not been studied very thoroughly in this work. Nevertheless, comparisons between experimental and calculated analyzing powers for proton elastic (Fig. 2) and neutron elastic (Fig. 3) scattering exhibit no apparent defects that could be attributed to the isovector SO OMP components. On the other hand, QE (p,n) analyzing powers [Figs. 5(c) and 9(d)] are not reproduced as well as the corresponding differential cross sections by our calculations. Nevertheless, the quality of agreement with data remains comparable to that exhibited in other studies [33,46,49,72]. Moreover, our tests have shown that the (p,n) analyzing powers calculated using the SO transition potential as described in Sec. III are virtually indistinguishable from the results of a calculation performed using no SO transition potential at all. A weak isospin component in the SO potential is consistent with other findings [69]. Also, as expected [33,69,72,73], the sign of the real isovector component of our SO potential is opposite that of the central isovector component. Finally, relativistic approaches [74] indicate that SO potentials near drip lines are considerably different from their stability valley counterparts. Since the SO components used in our approach have been tested only in selected cases of nuclei off the stability line [15,16], caution should be exercised in using these SO components with the more exotic systems.

Another topic that has not been fully developed so far in this paper is the OMP at low energies ($E<1$ MeV). While Fig. 4 gives a good idea of the quality of predictions at low energy, further tests are needed to assess the validity of our SM OMP in this energy range. One such test is the comparison between experimental and calculated values for the potential scattering radius (R') and the *s*- and *p*-wave neutron strength functions (S_0 and S_1) in the keV region. This comparison was performed for many of the target nuclei studied here, and we have found that R', S_0, and S_1 experimental values [75] are well predicted by our SM OMP analyses. For example, in the Sn region where S_0 is very weak, the S_0 values calculated with our SM OMP agree with the magnitude of experimental S_0 values. Other calculations [76] strongly overestimate these S_0 values. Moreover, our S_0 calculations predict a very slow decrease of S_0 with increasing Sn mass [$S_0(^{112}\mathrm{Sn})=0.411\times10^{-4}$, $S_0(^{124}\mathrm{Sn})=0.391\times10^{-4}$], a trend more in agreement with the data than is the increasing trend exhibited by other OMP calculations [75]. Note that the only OMP study [77] that accounts for S_0 details with the Sn isotopes does so by using unusually large imaginary isovector terms; qualitatively agreeing with the strong imaginary isovector enhancement present in our study. For the R' and S_1 observables, both the previous OMP study [75] and our SM OMP produce equally good descriptions of experimental results.

The last question that we discuss is the peculiar case of ^{40}Ca. For neutrons incident on ^{40}Ca between 10 and 20 MeV, the calculated neutron elastic differential cross sections tend to underestimate the experimental data at backward angles. While the change of imaginary potential depth needed to account for the data is well within our uncertainty

range, it is puzzling that this self-conjugate nucleus is not an excellent example for our Lane-consistent model. Note that a special case was made [5] for low energy ($E<20$ MeV) neutron scattering from this nucleus and tentatively attributed to double-shell closure effects. In the present context, a possible explanation could be an ambiguity in the balance between the imaginary isoscalar and isovector OMP components for $10\leqslant E\leqslant 20$ MeV. A way to remove this ambiguity would be to completely test the isovector terms of our SM OMP [i.e., testing proton and neutron elastic and (p,n) scattering at the same time] between 10 and 20 MeV. However, this is a difficult task since at low energy, compound (p,n) contributions can become so important that comparisons with data may be very dependent on compound nucleus parameters. Another possible explanation involves charge-symmetry breaking [78–80], but such a study is outside the scope of this work.

VI. SUMMARY AND CONCLUSIONS

We have specified a new spherical, Lane-consistent, semimicroscopic OMP built upon the density dependence of the JLM [11] NM OMP and energy-dependent potential depth normalizations factors that are adjusted phenomenologically and parametrized separately for the real isoscalar, real isovector, imaginary isoscalar, and imaginary isovector components of the OMP. This adjustment is performed in order to maximize the agreement between calculated and measured proton and neutron elastic scattering, QE (p,n) scattering, and reaction observables. To achieve that, the isovector components of the OMP were renormalized by a sizable factor (of the order of 1.5). The other key ingredient for building OMPs for finite nuclei is the description of nuclear densities used in the ILDA. In this work radial nuclear densities calculated in the HFB or HF+RPA framework, with Gogny's D1S force, have been used with success. Together, the nuclear structure information calculated with D1S and the revised NM OMP linked by the ILDA constitute what we designate as the JLMB (JLM+Bruyères) model.

We have shown that the JLMB OMP can account for a wide range of nucleon scattering and reaction observables, over the energy range from 1 keV to 200 MeV, and for spherical and near-spherical target nuclei from ^{40}Ca to ^{209}Bi. The good agreement between calculated and measured QE (p,n) scattering cross sections shows that the strengths of the isovector components of our OMP are of the right magnitude. Note that accounting simultaneously for the proton and neutron elastic and (p,n) cross sections constitutes a very stringent test for a Lane-consistent OMP [23]. Note also that the JLMB potential, which involves no more adjusted parameters than did our previous one [5], passes this test.

The large renormalization (about 1.5) of the isovector components necessary for the construction of a Lane-consistent, JLM-based OMP which accounts for proton and neutron elastic and QE (p,n) observables confirms the presumption [15,18,19] that the isovector components of the original JLM OMP are too weak. In the process, the strengths of the isovector components of the JLMB OMP have been determined, between 20 and 50 MeV, within total uncertainties of 11.5% and 20% for the real and imaginary components, respectively. The above uncertainties may be reduced when model-independent neutron density measurements are available from experiments such as of parity violating electron scattering measurements [81]. With those we could disentangle the uncertainties related to the model-dependent nuclear densities used in our approach from any intrinsic to the folding interaction itself.

QE (p,n) scattering calculations using the JLMB model have been shown to be sensitive to the nuclear structure information of the proton and neutron densities ρ_p and ρ_n, thus creating a link between experimental nucleon scattering observables and nuclear structure information. Likewise the descriptions of nuclear structure (HFB and HF+RPA calculations with Gogny D1S force) used in the JLMB OMP have been shown to be accurate representations of the radial proton and neutron distributions as may be inferred from data.

Comparisons with other OMPs, on the basis of volume integrals, mostly are inconclusive due to the strong influence of the different radial shapes exhibited by the OMPs we evaluate. Yet considering the size of uncertainties, a semiquantitative agreement is observed between our predictions and moduli extracted from other approaches. On the other hand, calculated nucleon mean free paths [20,70] are in good agreement with the JLMB OMP predictions. More precisely, for densities and asymmetry parameters that can be probed by scattering a nucleon off a nucleus within the drip lines, the agreement between the JLMB mean free paths and those of Ref. [20] is very good. This is encouraging if the JLMB OMP is to be used in applications that demand nuclear data far from stability (i.e., accelerator driven systems), since this comparison shows that for nuclei between drip lines the JLMB OMP isovector central components are well calibrated. These results also suggest that it would be useful to extend the BHF calculation in asymmetric nuclear matter [20] in a similar way to what was done with the original JLM approach. The added advantage is that such would be completely microscopic and so comparable with other studies of nucleon-nucleus elastic scattering that do not use phenomenological additions [1–4].

Finally, extending this spherical SM OMP study, in a systematic manner, to deformed and deformable nuclei should be quite straightforward as this extension has already been tested for the SM OMP [5], for rigid rotators [14], and for soft deformable, stable and unstable nuclei [15,16].

ACKNOWLEDGMENTS

We wish to express our gratitude J. Dechargé and S. Péru for providing us with the RPA densities shown in this paper. We are indebted to Professor J. Rapaport for his useful insight pertinent to (p,n) reactions at medium energies. Finally, the authors also want to thank J. Raynal for his constant support of the ECIS code.

[1] K. Amos, P. J. Dortmans, and S. Karataglidis, J. Phys. G **23**, 183 (1997); P. J. Dortmans, K. Amos, S. Karataglidis, and J. Raynal, Phys. Rev. C **58**, 2249 (1998); P. K. Deb, K. Amos, and S. Karataglidis, *ibid.* **62**, 037601 (2000); K. Amos, P. J. Dortmans, H. V. von Geramb, S. Karataglidis, and J. Raynal, *Advances in Nuclear Physics*, Vol. 25, edited by J. W. Negele and E. W. Vogt (Plenum, New York, 2000), and references therein.

[2] F. Sammarucca, E. J. Stephenson, and K. Jiang, Phys. Rev. C **60**, 064610 (1999); F. Sammarucca, E. J. Stephenson, K. Jiang, J. Liu, C. Olmerm, A. K. Opper, and S. W. Wissink, *ibid.* **61**, 014309 (2000).

[3] Ch. Elster and S. P. Weppner, Phys. Rev. C **57**, 189 (1998); S. P. Weppner, Ch. Elster, and D. Huber, *ibid.* **57**, 1378 (1998); C. R. Chinn, Ch. Elster, R. M. Thaler, and S. P. Weppner, *ibid.* **51**, 1033 (1995); Ch. Elster, S. P. Weppner, and C. R. Chinn, *ibid.* **56**, 2080 (1997).

[4] H. F. Arellano, F. A. Brieva, and W. G. Love, Phys. Rev. C **52**, 301 (1995); H. F. Arellano, F. A. Brieva, M. Sander, and H. V. von Geramb, *ibid.* **54**, 2570 (1996).

[5] E. Bauge, J. P. Delaroche, and M. Girod, Phys. Rev. C **58**, 1118 (1998).

[6] D. T. Koa and G. R. Satchler, Nucl. Phys. **A668**, 3 (2000).

[7] K. A. Brueckner and J. Dabrowski, Phys. Rev. **134**, B722 (1964).

[8] J. P. Jeukenne, A. Lejeune, and C. Mahaux, Phys. Rep., Phys. Lett. **25C**, 83 (1976).

[9] J. P. Jeukenne, A. Lejeune, and C. Mahaux, Phys. Rev. C **10**, 1391 (1974).

[10] J. P. Jeukenne, A. Lejeune, and C. Mahaux, Phys. Rev. C **15**, 10 (1977).

[11] J. P. Jeukenne, A. Lejeune, and C. Mahaux, Phys. Rev. C **16**, 80 (1977).

[12] R. V. Reid, Ann. Phys. (N.Y.) **50**, 525 (1972).

[13] J. S. Bell and E. J. Squires, Phys. Rev. Lett. **3**, 96 (1959).

[14] E. Bauge, J. P. Delaroche, M. Girod, G. Haouat, J. Lachkar, Y. Patin, J. Sigaud, and J. Chardine, Phys. Rev. C **61**, 034306 (2000).

[15] F. Maréchal *et al.*, Phys. Rev. C **60**, 034615 (1999).

[16] H. Sheit *et al.*, Phys. Rev. C (to be published).

[17] A. M. Lane, Nucl. Phys. **35**, 676 (1962).

[18] F. S. Dietrich and F. Petrovich, in *Neutron-Nucleus Collisions: a Probe of Nuclear Structure*, edited by J. Rapaport, R. W. Finlay, S. M. Grimes, and F. S. Dietrich, AIP Conf. Proc. No. 124 (AIP, New York, 1984), p. 90.

[19] M. D. Cortina-Gil *et al.*, Nucl. Phys. **A641**, 263 (1998).

[20] W. Zuo, I. Bombaci, and U. Lombardo, Phys. Rev. C **60**, 024605 (1999); I. Bombaci and U. Lombardo, *ibid.* **44**, 1892 (1991).

[21] J. J. Kelly *et al.*, Phys. Rev. C **44**, 2602 (1991) and references therein.

[22] H. Seifert *et al.*, Phys. Rev. C **47**, 1615 (1993) and references therein.

[23] J. D. Carlson, D. A. Lind, and C. D. Zafiratos, Phys. Rev. Lett. **30**, 99 (1973).

[24] J. Dechargé and D. Gogny, Phys. Rev. C **21**, 1568 (1980); J. Dechargé, L. Sips, and D. Gogny, Phys. Lett. **98B**, 229 (1981); J. Dechargé and L. Sips, Nucl. Phys. **A407**, 1 (1983).

[25] J. F. Berger, M. Girod, and D. Gogny, Comput. Phys. Commun. **63**, 365 (1990) and references therein.

[26] M. Girod and P. G. Reinhard, Nucl. Phys. **A384**, 179 (1982); B. Frois *et al.*, Phys. Lett. **122B**, 347 (1982); W. Boeglin *et al.*, Nucl. Phys. **A477**, 399 (1988); R. K. J. Sandor, H. P. Blok, M. Girod, M. N. Harakeh, C. W. de Jager, and H. de Vries, *ibid.* **A551**, 349 (1993); R. K. J. Sandor, H. P. Blok, M. Girod, M. N. Harakeh, C. W. de Jager, V. Yu. Ponomarev, and H. de Vries, *ibid.* **A551**, 378 (1993); Z. Patyk, A. Baran, J. F. Berger, J. Dechargé, J. Dobaczewski, P. Ring, and A. Sobiczewski, Phys. Rev. C **59**, 704 (1999).

[27] B. Frois, C. N. Papanicolas, and S. E. Williamson, in *Modern Topics in Electron Scattering*, edited B. Frois and I. Sick (World Scientific, Singapore, 1991), p. 352.

[28] W. T. H. van Oers, Huang Haw, N. E. Davison, A. Ingermarson, B. Fagersrom, and G. Tibell, Phys. Rev. C **10**, 307 (1974).

[29] J. Raynal, CEA Report No CEA-N-2772, 1994.

[30] J. D. Anderson, C. Wong, and J. W. McClure, Phys. Rev. **138**, B615 (1965).

[31] G. R. Satchler, R. M. Drisko, and R. H. Bassel, Phys. Rev. **136**, B637 (1964).

[32] R. R. Scheerbaum, Nucl. Phys. **A257**, 77 (1976).

[33] J. Gosset, B. Mayer, and J. L. Escudié, Phys. Rev. C **14**, 878 (1974).

[34] H. W. Fielding, L. D. Rickertsen, P. D. Kuntz, D. A. Lind, and C. D. Zafiratos, Phys. Rev. Lett. **33**, 226 (1974).

[35] J. D. Carlson, C. D. Zafiratos, and D. A. Lind, Nucl. Phys. **A249**, 29 (1975); R. F. Bentley, J. D. Carlson, D. A. Lind, R. B. Perkins, and C. D. Zafiratos, Phys. Rev. Lett. **27**, 1081 (1971).

[36] S. D. Schery, D. A. Lind, and H. Wieman, Phys. Rev. C **14**, 1800 (1976).

[37] S. D. Schery, D. A. Lind, H. W. Fielding and C. D. Zafiratos, Nucl. Phys. **A234**, 109 (1974).

[38] S. M. Grimes, C. H. Poppe, J. D. Anderson, J. C. Davis, W. H. Dunlop, and C. Wong, Phys. Rev. C **11**, 158 (1975).

[39] J. D. Anderson, V. R. Brown, R. W. Bauer, B. A. Pohl, C. H. Poppe, S. Stamer, E. Mordhorst, W. Scobel, S. M. Grimes, and V. A. Madsen, Phys. Rev. C **41**, 1993 (1990).

[40] S. D. Schery, D. A. Lind, and C. D. Zafiratos, Phys. Lett. **97B**, 25 (1980).

[41] C. J. Batty, B. E. Bonner, E. Friedman, C. Tshalar, L. E. Williams, A. S. Clough, and J. B. Hunt, Nucl. Phys. **A116**, 643 (1968).

[42] K. Maeda, H. Orihara, T. Murakami, S. Nishihara, T. Nakagawa, K. Miura, and H. Ohnuma, Nucl. Phys. **A403**, 1 (1983).

[43] S. D. Schery, S. M. Austin, A. Galonski, L. E. Young, and U. E. P. Berg, Phys. Lett. **79B**, 30 (1978).

[44] R. R. Doering, D. M. Patterson, and A. Galonski, Phys. Rev. C **12**, 378 (1975).

[45] D. E. Bainum, J. Rapaport, C. D. Goodman, D. J. Horen, C. C. Foster, M. B. Greenfield, and C. A. Goulding, Phys. Rev. Lett. **44**, 1751 (1980).

[46] B. D. Anderson, T. Chittrakarn, A. R. Baldwin, A. Fazely, C. Lebo, R. Madey, J. W. Watson, and C. C. Foster, Phys. Rev. C **34**, 422 (1986).

[47] B. D. Anderson, M. Mostajabodda'vati, C. Lebo, R. J. McCarty, L. Garcia, J. W. Watson, and R. Madey, Phys. Rev. C **43**, 1630 (1991).

[48] B. D. Anderson, T. Chittrakarn, A. R. Baldwin, C. Lebo, R.

Madey, J. W. Watson, B. A. Brown, and C. C. Foster, Phys. Rev. C **31**, 1147 (1985).
[49] B. C. Clark, S. Hama, E. Sugarbaker, M. A. Franey, R. L. Mercer, L. Ray, W. G. Hoffmann, and B. D. Serot, Phys. Rev. C **30**, 314 (1984).
[50] C. Gaarde, J. Rapaport, T. N. Taddeucci, C. D. Goodman, C. C. Foster, D. E. Bainum, C. A. Goulding, M. B. Greenfield, D. J. Horen, and E. Sugarbaker, Nucl. Phys. **A369**, 258 (1981).
[51] J. Schwinger, Phys. Rev. **73**, 407 (1948); W. Heckrotte, *ibid.* **101**, 1406 (1956); N. Alexander, K. Amos, and L. Berge, Aust. J. Phys. **47**, 681 (1994); N. Alexander and K. Amos, *ibid.* **49**, 633 (1996).
[52] M. Ibaraki, H. Nakashima, S. Meigo, M. Baba, T. Miura, Y. Hirasawa, T. Hiroshi, T. Aoki, and S. Tanaka, in *Proceedings of the 1999 Symposium on Nuclear Data*, edited by N. Yamano and T. Fukahori (JAERI, Tokai, 2000), p. 243.
[53] V. A. Madsen, V. R. Brown, S. M. Grimes, C. H. Poppe, J. D. Anderson, J. C. Davis, and C. Wong, Phys. Rev. C **13**, 548 (1976).
[54] J. D. Anderson, R. W. Bauer, V. R. Brown, S. M. Grimes, V. A. Madsen, B. A. Pohl, C. H. Poppe, and W. Scobel, Phys. Rev. C **38**, 1601 (1988).
[55] G. W. Hoffman, W. H. Dunlop, G. J. Igo, J. G. Kulleck, C. A. Witten, and W. R. Coker, Phys. Lett. **40B**, 453 (1972).
[56] J. Rapaport, in *The (p,n) Reaction and the Nucleon Nucleon Force*, Proceedings of the Conference on the (p,n) Reaction and the Nucleon Nucleon Force, Telluride, CO, 1979, edited by C. D. Goodman, S. M. Austin, S. Bloom, J. Rapaport, and G. R. Satchler (Plenum, New York, 1979), p. 233.
[57] G. T. Garvey and P. S. Miller, Phys. Lett. **28B**, 244 (1968); P. S. Miller, Ph.D. thesis, Princeton University, 1968.
[58] C. H. Poppe, in *The (p,n) Reaction and the Nucleon Nucleon Force* [56], p. 461.
[59] J. Dechargé, M. Girod, D. Gogny, and B. Grammaticos, in *Proceedings of the Symposium on Perspectives in Electro- and Photo-Nuclear Physics*, edited by A. Gérard and C. Samour (North-Holland, Amsterdam, 1981), p. 203c.
[60] B. Frois, J. B. Bellicard, J. M. Cavedon, M. Huet, P. Leconte, P. Ludeau, A. Nakada, Phan Zuan Ho, and I. Sick, Phys. Rev. Lett. **38**, 152 (1977).
[61] V. E. Starodubsky and N. M. Hintz, Phys. Rev. C **49**, 2118 (1994).
[62] C. J. Batty, E. Friedmann, and G. W. Greenlees, Nucl. Phys. **A127**, 368 (1969).
[63] C. J. Batty *et al.*, Adv. Nucl. Phys. **19**, 1 (1989).
[64] A. Krasznahorkay *et al.*, Phys. Rev. Lett. **82**, 3216 (1999).
[65] W. G. Love and M. A. Franey, Phys. Rev. C **24**, 1073 (1981).
[66] C. D. Goodman, C. A. Gouldling, M. B. Greenfield, J. Rapaport, D. E. Bainum, C. C. Foster, W. G. Love, and F. Petrovich, Phys. Rev. Lett. **44**, 1755 (1980).
[67] J. Rapaport, in *The Interaction Between Medium Energy Nucleons in Nuclei*, edited by H. O. Meyer, AIP Conf. Proc. No. 97 (AIP, New York, 1982), p. 365.
[68] T. N. Taddeucci, C. A. Gouldling, T. A. Carey, B. C. Byrd, C. D. Goodman, C. Gaarde, J. Larsen, D. Horen, J. Rapaport, and E. Sugarbaker, Nucl. Phys. **A469**, 125 (1987).
[69] W. G. Love, in *The (p,n) Reaction and the Nucleon Nucleon Force* [56], p. 23.
[70] E. D. Cooper, S. Hama, B. C. Clark, and R. L. Mercer, Phys. Rev. C **47**, 297 (1993).
[71] B. C. Clark, E. D. Cooper, S. Hama, R. W. Finlay, and T. Adami, Phys. Lett. B **299**, 189 (1993).
[72] J. M. Moss, C. Brassard, R. Vyse, and J. Gosset, Phys. Rev. C **6**, 1698 (1972).
[73] F. Petrovich, in *Microscopic Optical Potential*, Proceedings of the Hamburg Topical Workshop on Nuclear Physics, Hamburg, 1978, edited by H. V. von Geramb (Springer-Verlag, Berlin, 1979), p. 155.
[74] M. Onsi, R. C. Nayak, J. M. Pearson, H. Freyer, and W. Stocker, Phys. Rev. C **55**, 3166 (1997).
[75] S. F. Mughabghab, M. Divadeenam, and N. E. Holden, *Neutron Cross Sections* (Academic, New York, 1981).
[76] B. Buck and F. Perey, Phys. Rev. Lett. **8**, 444 (1962).
[77] J. P. Delaroche, Ph.D. thesis, Orsay University, 1972; C. M. Newstead, J. P. Delaroche, and B. Cauvin, *Statistical Properties of Nuclei* (Plenum, New York, 1972), p. 367.
[78] R. P. DeVito, S. M. Austin, U. E. P. Berg, R. De Leo, and W. A. Sterrenburg, Phys. Rev. C **28**, 2530 (1983).
[79] J. S. Winfield, S. M. Austin, R. P. DeVito, U. E. P. Berg, Ziping Chen, and W. A. Sterrenburg, Phys. Rev. C **33**, 1 (1986).
[80] C. R. Howell, R. S. Pedroni, G. M. Honoré, K. Murphy, R. C. Byrd, G. Tungate, and R. L. Walter, Phys. Rev. C **38**, 1552 (1988).
[81] D. Vretenar, P. Finelli, A. Ventura, G. A. Lalazissis, and P. Ring, Phys. Rev. C **61**, 064307 (2000); T. Suzuki, *ibid.* **50**, 2815 (1994); T. W. Donnelly, J. Dubach, and I. Sick, Nucl. Phys. **A503**, 589 (1989); C. J. Horowitz, Phys. Rev. C **57**, 3430 (1998).